Chemical Science

ROYAL SOCIETY OF CHEMISTRY

EDGE ARTICLE

View Article Online
View Journal

Cite this: DOI: 10.1039/d6sc00009f

All publication charges for this article have been paid for by the Royal Society of Chemistry

Reductive-defect-suppressed titanium oxynitrides *via* Ca_3N_2-assisted topochemical nitridation

Yuki Sasahara, †[a] Kento Yoshii,†[a] Daichi Kato, [a] Issei Yamamoto,[b] Yusuke Tsutsui,[c] Kei Morisato,[a] Hikaru Takeuchi,[a] Tatsuya Tsumori,[a] Hiroshi Takatsu,[a] Satoshi Horike, [d] Shu Seki, [c] Kazuhiko Maeda [be] and Hiroshi Kageyama *[a]

Received 1st January 2026
Accepted 4th March 2026

DOI: 10.1039/d6sc00009f

rsc.li/chemical-science

Transition-metal oxynitrides are promising for photocatalysis and dielectric applications owing to their visible-light absorption and tunable band structures. Conventional ammonolysis, however, proceeds under reducing conditions that cause electron doping and limited compositional control. Here, we present a one-step, ammonia-free topochemical nitridation using Ca_3N_2 as a solid nitrogen source. $BaTiO_3$ reacts with Ca_3N_2 at 550 °C *via* a stoichiometric $3O^{2-}/2N^{3-}$ anion-exchange process to yield orange $BaTiO_{3-3x/2}N_x$ with Ti^{3+}-related reductive defects suppressed below detectable levels. The resultant oxynitrides exhibit tunable bandgaps, high crystallinity, and visible-light photoactivity, while the CaO byproduct can be readily removed by washing. This method establishes Ca_3N_2 as a safe and effective reagent for controlled, ammonia-free oxynitride synthesis.

Introduction

Mixed-anion oxides, which integrate distinct anions within a single oxide framework, offer a powerful strategy for engineering crystal and electronic structures beyond the limits of conventional oxides.[1] Among them, oxynitrides have attracted particular attention because the lower electronegativity of nitrogen raises the energy of the N 2p orbitals, thereby elevating the valence band maximum (VBM)[2] and enabling visible-light absorption. For example, partial nitridation of wide-bandgap oxides such as TiO_2 introduces N 2p states near the VBM, enhancing photocatalytic activity.[3] Pigments such as $Ca_{1-x}La_xTaO_{2-x}N_{1+x}$ exhibit tunable bandgaps (E_g = 2.0–2.4 eV),[4] whereas TaON and related compounds have been widely studied for solar water splitting and CO_2 reduction.[5,6] The high polarizability of N^{3-} also contributes to enhanced dielectric responses in $ATaO_2N$ (A = Ba, Sr),[7,8] expanding the functional scope of oxynitrides.

Despite these promising features, synthetic challenges remain. The most common method, ammonolysis, requires high-temperature treatment under flowing ammonia gas,[2,5] raising safety concerns[2] and offering limited control over reaction pathways[9,10] due to its *in situ* generation of highly reactive species (*e.g.*, NH_2, N, H). In transition-metal oxynitrides, the reducing environment often induces undesirable changes in oxidation state; for instance, partial reduction of Ti^{4+} to Ti^{3+} in $LaTiO_2N$ introduces mid-gap defect states that deteriorate photocatalytic performance,[11] unlike redox-stable Ta-based systems.[5] Topochemical nitridation using oxyhydride precursors (*e.g.*, $BaTiO_{2.4}H_{0.6} \rightarrow BaTiO_{2.4}N_{0.4}$) provides a milder alternative,[12] but residual Ti^{3+} species are still observed and can compromise optoelectronic properties.

Solid-state nitridation routes using nitrogen-containing precursors such as urea or C_3N_4 have been explored as safer, ammonia-free alternatives,[13–16] yielding oxynitrides including ABO_2N (A = Ba, Sr, Ca, B = Ta, Nb) and $LaTiO_2N$ at moderate temperatures (~700–800 °C). However, these processes proceed through complex, multi-step pathways involving intermediate phases (*e.g.*, $La_2O_2CN_2$ for $LaTiO_2N$, $SrCN_2$ for $SrTaO_2N$)[14,15] and often leave carbonaceous byproducts on particle surfaces, which deteriorate surface quality and catalytic performance.[17]

In this study, we report a safe, one-step, ammonia-free topochemical nitridation that uses Ca_3N_2 as a solid nitrogen source. Unlike most refractory nitrides, Ca_3N_2 has a relatively low melting point (1195 °C),[18] providing sufficient reactivity at moderate temperatures. Remarkably, reaction of $BaTiO_3$ with Ca_3N_2 at 550 °C yields $BaTiO_{3-3x/2}N_x$, with Ti^{3+}-related reductive defects suppressed below detectable levels. After removal of the CaO byproduct, the resulting powders exhibit a bright orange color, in contrast to the bluish-green of Ti^{3+}-containing oxynitrides obtained *via* ammonolysis.[19] Structural analysis

[a]Department of Energy and Hydrocarbon Chemistry, Graduate School of Engineering, Kyoto University, Kyoto 615-8510, Japan. E-mail: kage@scl.kyoto-u.ac.jp
[b]Department of Chemistry, School of Science, Institute of Science Tokyo, Tokyo 152-8550, Japan
[c]Department of Molecular Engineering, Graduate School of Engineering, Kyoto University, Kyoto 615-8510, Japan
[d]Department of Chemistry, Graduate School of Science, Kyoto University, Kyoto 606-8502, Japan
[e]Research Center for Autonomous Systems Materialogy, Institute of Science Tokyo, Kanagawa 226-8501, Japan
† These authors contributed equally.

supports homogeneous N^{3-} incorporation consistent with a stoichiometric $3O^{2-}/2N^{3-}$ anion-exchange mechanism. The resulting oxynitride exhibits a distinct visible-light absorption edge originating from N 2p-derived states and enhanced photocatalytic activity as a photoanode. These findings demonstrate that Ca_3N_2 enables controlled, ammonia-free nitridation and establish a general topochemical strategy for minimizing reductive defect formation in oxynitrides, providing a practical route to functional materials with improved stability and optoelectronic properties.

Results and discussion

A mixture of cubic $BaTiO_3$ powder (~100 nm) and Ca_3N_2 (1 : 3 molar ratio) was heated at 550 °C under vacuum for one week. Powder X-ray diffraction (XRD) revealed a slightly expanded cubic phase ($a = 4.01557(5)$ Å) compared to pristine $BaTiO_3$ ($a = 4.01433(6)$ Å). Residual Ca_3N_2, CaO byproduct, and trace impurities were completely removed by sequential washing with NH_4Cl in methanol followed by water (Fig. S1). The purified product exhibited an orange color, distinct from the white precursor, indicating partial substitution of O^{2-} with N^{3-} without evidence of Ti^{4+} reduction (Fig. 1, inset).

Conventional ammonolysis[19] and two-step oxyhydride routes[12] typically yield bluish-green products originating from Ti^{3+} defects (Fig. 1, inset). In sharp contrast, the Ca_3N_2-treated samples show no detectable Ti^{3+} signatures. Photoluminescence (PL) measurements further confirm the negligible defect density, showing strong band-edge emission around 2.0 eV, whereas the ammonolysis-derived sample shows weak and broadened emission (Fig. S2), indicative of pronounced nonradiative recombination. Electron paramagnetic resonance (EPR) and Ti L-edge soft X-ray absorption spectroscopy (XAS) measurements do not reveal measurable Ti^{3+} signatures in the Ca_3N_2-treated samples within their detection limits (Fig. S3).[20] These findings are consistent with a stoichiometric 3 : 2 anion-exchange mechanism:

$$BaTiO_3 + 0.5x\ Ca_3N_2 \rightarrow BaTiO_{3-3x/2}N_x + 1.5x\ CaO \quad (1)$$

To investigate the reaction kinetics, the heating duration for the $BaTiO_3$–Ca_3N_2 reaction was varied from 24 h to 2 weeks. Powder XRD revealed a gradual shift of diffraction peaks toward lower angles with increasing time, consistent with lattice expansion accompanying progressive nitrogen incorporation (Fig. 2a).[12] The diffraction peaks remained sharp under all conditions, indicating preservation of crystallinity (Fig. S4). Correspondingly, the washed samples exhibited a gradual color change from yellow to orange with prolonged heating (Fig. 2b),

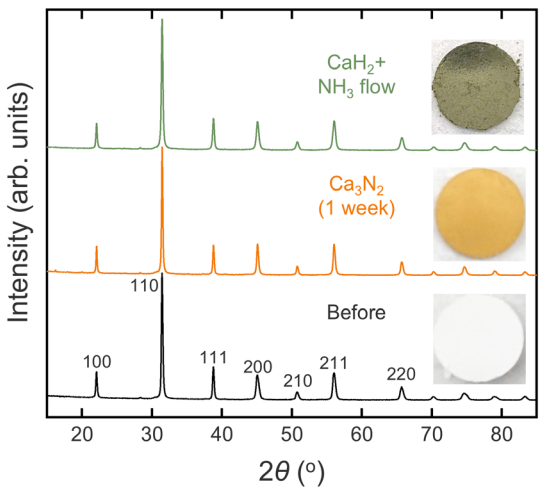

Fig. 1 Powder XRD patterns of $BaTiO_{3-3x/2}N_x$ samples (~100 nm) before and after reaction with Ca_3N_2 at 550 °C for one week, followed by washing to remove residual Ca_3N_2 and the CaO byproduct (Fig. S1). For comparison, $BaTiO_{2.53}N_{0.31}$ synthesized *via* ammonolysis of $BaTiO_{2.53}H_{0.47}$ is shown at the top.[12] The inset photographs highlight the color change from white (pristine $BaTiO_3$) to orange (no detectable Ti^{3+}) and green (indicating the presence of Ti^{3+} defects), illustrating the contrast between the two reaction routes.

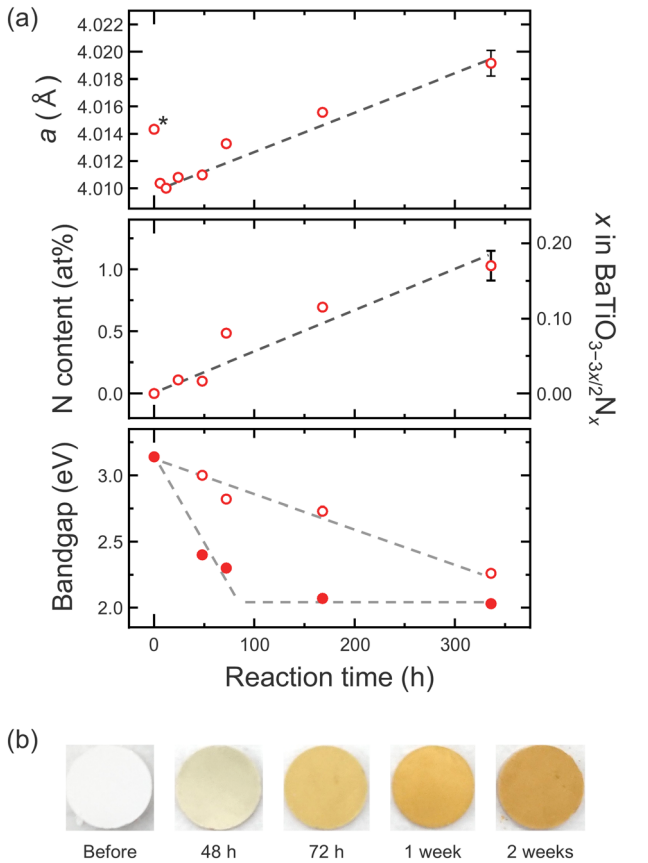

Fig. 2 (a) (top) Lattice constant *a*, (middle) nitrogen content, and (bottom) bandgap of $BaTiO_{3-3x/2}N_x$ as a function of reaction time with Ca_3N_2 at 550 °C (Table S1). The asterisk denotes a precursor undergoes lattice shrinkage readily upon heat treatment, a behavior typical of nanocrystalline $BaTiO_3$ (Table S2).[21–23] In the bottom panel, filled and open symbols represent the first (lower-energy) and second (higher-energy) absorption steps derived from Tauc plots; both are assigned as indirect transitions. Dashed lines are guides to the eye. (b) Photographs of $BaTiO_{3-3x/2}N_x$ samples reacted with Ca_3N_2 for different durations, after washing to remove residual Ca_3N_2 and the CaO byproduct, showing a gradual color change with increasing reaction time.

supporting progressive $3O^{2-}/2N^{3-}$ substitution without detectable Ti^{4+} reduction. Combustion analysis gave a maximum nitrogen content of $x = 0.20$ ($BaTiO_{2.71}N_{0.20}$), which lies between values typically obtained for ammonolysis-derived samples ($x \approx$ 0.1)19 and oxyhydride routes ($x \approx 0.4$).[12]

To assess diffusion limitations, particle-size effects were examined. Smaller particles (≤100 nm) retained sharp diffraction peaks and higher nitrogen incorporation, whereas larger particles (≥300 nm) exhibited peak broadening and reduced nitrogen content (Fig. S5), consistent with diffusion-limited nitridation. Spatial homogeneity was further confirmed by X-ray photoelectron spectroscopy (XPS) depth profiling of a ~50 nm $BaTiO_3$ thin film treated under identical conditions, which shows a uniform nitrogen signal across the film thickness (Fig. S6). In contrast, increasing the reaction temperature to 650 °C led to over-reaction and TiN forming (Fig. S7), indicating a narrow temperature window for controlled nitridation.

In oxynitrides, the higher energy N 2p orbitals relative to O 2p results in an upward shift of the valence band maximum and a reduced bandgap.[2–5] Consistent with this, the UV-vis diffuse reflectance spectra of $BaTiO_{3-3x/2}N_x$ display an additional long-wavelength absorption compared with $BaTiO_3$ (Fig. S8a), in line with the observed color change. Tauc analysis indicates indirect bandgap transitions for all samples, with the bandgap narrowing from 3.14 eV to 2.03 eV after one week of reaction (Fig. 2a). Prolonged heating did not further reduce the bandgap, suggesting that bandgap narrowing had reached saturation. However, the absorption intensity in near-edge region gradually increased, indicating subtle evolution of the electronic states near the band edge (Fig. S8b).

These results demonstrate that Ca_3N_2 serves as an effective reagent for topochemical $3O^{2-}/2N^{3-}$ anion exchange, enabling nitrogen incorporation while suppressing reductive electron doping. In conventional oxygen–nitrogen exchange reactions, reductive conditions are unavoidable: ammonolysis generates highly reactive species (*e.g.*, NH_2, NH, N, and H) that readily reduce transition-metal cations,[9] while in the two-step oxyhydride route, electrons introduced into intermediate phases (*e.g.*, $BaTiO_{3-x}H_x$) cannot be completely removed during reoxidation, leaving residual reduced species (*e.g.*, Ti^{3+}, d^1) in the final product.[12] In contrast, the Ca_3N_2-mediated reaction proceeds in the absence of a reducing atmosphere, allowing precise nitrogen substitution while maintaining Ti in a predominantly d^0 electronic configuration within the detection limits of our measurements.

This method offers four key advantages. (i) The formation of the highly stable byproduct CaO ($\Delta G_f^\circ = -602.5$ kJ mol^{-1}) thermodynamically drives the reaction (eqn (1)), analogous to CaH_2-mediated oxyhydride synthesis.[24–26] (ii) Ca_3N_2 possesses an unusually low melting point (1195 °C), far below those of typical nitrides such as ZrN (2952 °C) and VN (2050 °C) (Table S2),[18,27] affording sufficient reactivity at moderate temperatures.[28,29] Notably, Li_3N, despite its lower melting point (845 °C), does not enable controlled nitridation under comparable conditions (Fig. S9), highlighting that melting point alone is insufficient and that the thermodynamic driving force for oxygen removal is critical. (iii) The reaction proceeds in the absence of hydrogen, avoiding the formation of reductive hydrogen species (*e.g.*, NH_2, NH, H_2) typical of ammonolysis and thereby suppressing Ti^{3+}-related defects. (iv) The CaO byproduct can be readily removed by simple wet-chemical treatment, yielding a clean oxynitride without residual surface contaminants (Fig. S1), unlike carbon-based reagents such as urea.[17]

The orange $BaTiO_{2.73}N_{0.18}$ sample, with a bandgap and band-edge alignment consistent with visible-light-driven water splitting, was evaluated by photoelectrochemical (PEC) measurements (Fig. S10). All PEC measurements were performed under identical conditions to allow direct comparison of the photoresponse behavior among samples. Electrodes were prepared by depositing $BaTiO_3$ (control) or $BaTiO_{2.73}N_{0.18}$ onto fluorine-doped tin oxide (FTO) substrates, followed by irradiation with visible light ($\lambda > 400$ nm). As expected, pristine $BaTiO_3$ showed negligible photocurrent, whereas $BaTiO_{2.73}N_{0.18}$ generated a stable anodic photocurrent of 1.63 μA cm^{-2} at +1.0 V *vs.* RHE, about five times higher than that of the control, indicating improved visible-light photoresponse upon nitridation (Fig. 3a). The photocurrent remained stable under chopped light illumination (Fig. 3b), with reproducible on/off responses synchronized with light irradiation, confirming the photoelectrochemical origin of the signal.

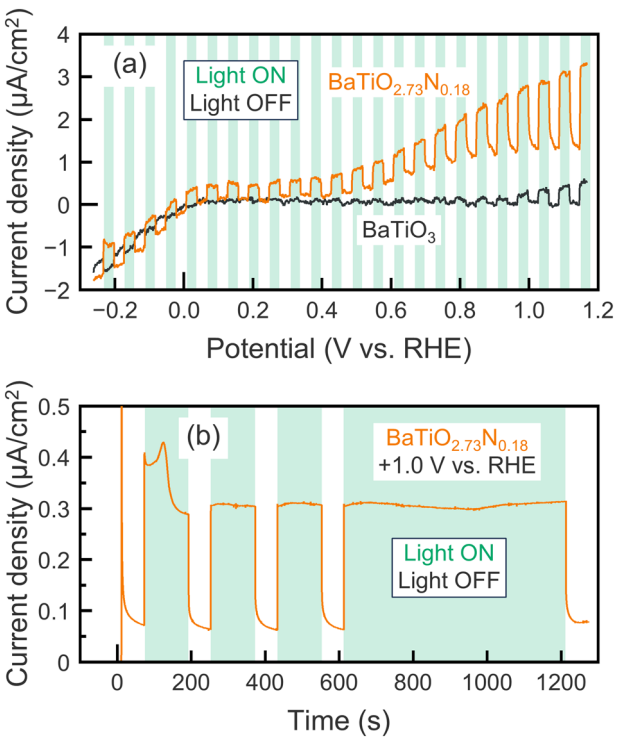

Fig. 3 (a) Current–voltage curves measured in 0.1 M Na_2SO_4 aqueous solution (pH 5.9) under intermittent visible-light irradiation for $BaTiO_3$/FTO and $BaTiO_{2.73}N_{0.18}$/FTO electrodes. Scan rate: 20 mV s^{-1}. (b) Transient (light on/off) photocurrent responses of the $BaTiO_{2.73}N_{0.18}$/FTO electrode at +1.0 V *vs.* RHE in 0.1 M Na_2SO_4. Clear and reproducible on/off responses are observed upon light modulation. The absolute photocurrent density is smaller than that in (a), as this potentiostatic measurement reflects the steady-state response after transient capacitive components relax.[33–35]

For comparison, the sample prepared *via* the oxyhydride route ($BaTiO_{2.53}N_{0.31}$) showed a higher initial photocurrent but suffered rapid degradation under illumination (Fig. S11). This decay is attributed to a higher defect density, which can facilitate nonradiative recombination and photocorrosion.[30] In contrast, PL measurements of the Ca_3N_2-treated sample show no detectable mid-gap emission, supporting a lower density of recombination-active defects (Fig. S2). These results suggest that the photocatalytic performance could be further improved by enhancing charge extraction, for instance, through cocatalyst loading or facet engineering.[31,32] Indeed, in Al-doped $SrTiO_3$, cocatalyst loading enables efficient utilization of photogenerated carriers in surface reactions, yielding a highly efficient photocatalyst with a quantum efficiency approaching 100%.[31]

Conclusions

In summary, we have developed a one-step, ammonia-free topochemical nitridation route for synthesizing the oxynitride $BaTiO_{3-3x/2}N_x$ using Ca_3N_2 as a solid nitrogen source. The reaction proceeds at 550 °C *via* a stoichiometric $3O^{2-}/2N^{3-}$ anion-exchange process, with Ti^{3+}-related reductive defects suppressed below detectable levels, yielding phase-pure orange powders with tunable bandgaps. The resulting oxynitride exhibits stable visible-light photoactivity without photodegradation, consistent with its low defect density and well-preserved crystallinity. This combination of controlled anion exchange, defect suppression, and mild hydrogen-free processing establishes Ca_3N_2 as a practical and broadly applicable nitrogen source for the synthesis of photoactive semiconductors and related optoelectronic materials.

Experimental

Polycrystalline $BaTiO_{3-3x/2}N_x$ samples were synthesized by a topochemical reaction using $BaTiO_3$ powders with particle sizes of 50, 100, 300, and 500 nm (KSZ-50, BT-01, BT-03, and BT-05, Sakai Chemical Industry) and a 3 molar excess of Ca_3N_2 (Aldrich, 99%). The powders were ground and pelletized in an N_2-filled glovebox. The pellets were sealed in Pyrex tubes under vacuum (<5 Pa) and heated at 550 °C and 650 °C for 6 hours to 2 weeks. After cooling, the pellets were crushed and washed with 0.1 M NH_4Cl/MeOH and 0.1 M NH_4Cl/H_2O to remove residual Ca_3N_2 and the by-product CaO. The samples were then dried under vacuum. This procedure follows previous protocols for $BaTiO_{3-x}H_x$.[24–26]

For comparison, alternative nitridation reagents, VN (Kojundo Chemical Lab, 98%), ZrN (Kojundo Chemical Lab, 99%), and Li_3N (Aldrich, 99.5%), were also tested. Each reagent was mixed with 100 nm $BaTiO_3$ powder (BT-01) in a 6 molar excess and pelletized. The VN- and ZrN-containing pellets were heated at 550 °C for 2 weeks, whereas the Li_3N-containing pellets were treated at 350, 450, and 550 °C (2 weeks each). The products were analyzed without washing. As a control, pelletized $BaTiO_3$ (BT-01) was subjected to identical heat treatment (550 °C for 2 weeks) without nitridation reagents.

Powder X-ray diffraction (XRD) measurements were carried out at room temperature using a Rigaku SmartLab with Cu Kα radiation. The XRD data were analyzed by Le Bail fitting using Jana2006.[36] Elemental analysis was conducted using a Micro Corder JM11 (Elemental Analysis Section, Institute for Chemical Research, Kyoto University). Approximately 1.5–2 mg of each sample was combusted at 950 °C for 5 min in a helium stream with auxiliary oxygen and a copper oxide oxidizer. Scanning electron microscopy (SEM) images were acquired using a JEOL JSM-IT500HR to examine particle morphology. Elemental compositions were analyzed by energy-dispersive X-ray spectroscopy (EDX) using an Oxford X-act detector attached to a Hitachi S-3400N SEM.

EPR measurements were performed using a JEOL JES-FA200 X-band spectrometer (9.413 GHz), with Mn/MgO as an internal standard. A powder sample (2.8 mg) was loaded into a quartz tube and placed in the microwave cavity. The microwave power and magnetic-field modulation amplitude were set to 1 mW and 0.2 mT, respectively. Ti L-edge soft X-ray absorption spectroscopy (XAS) was conducted in total electron yield (TEY) and partial fluorescence yield (PFY) modes at BL-12 A of the Photon Factory (KEK), Japan. Measurements were carried out under high vacuum ($\sim 10^{-5}$ Pa) at room temperature. The spectra were normalized to the incident photon flux using the upstream mirror current (I_0). UV-visible diffuse reflectance spectra were collected with a Jasco V-650 spectrophotometer, and bandgap energies were estimated from Tauc plots.

Photoluminescence (PL) measurement was carried out in the following way. The powder samples were fixed onto a quartz plate with CYTOP polymer matrix (CTL-809M) and loaded in a closed-cycle helium cryostat for variable temperature measurement. The sample was photo-excited by a picosecond diode laser (405 nm, LDB-160C-405, Tama-denshi). Due to its faint photoluminescence, it was guided to a photon counter (C16533, Hamamatsu Photonics) through a series of parabolic mirrors and counted using a universal frequency counter (53230A, Keysight) in a reflective configuration. In order to select monitor wavelength, 10 nm band-pass filters were used (FBH-XXX-10, XXX = 450, 480, 500, 532, 600, and 650, Thorlabs). The representative quantum yields of the photon counter were used for sensitivity correction.

Ar^+ sputtering-assisted X-ray photoelectron spectroscopy (XPS) depth profiling was performed to examine the nitrogen depth distribution using an epitaxial $BaTiO_3$ thin film as a model system. The film was grown on an MgO(100) substrate (Shinkosha Corp.) by pulsed laser deposition using a Nd:$Y_3Al_5O_{12}$ laser (266 nm, 2.5 J cm^{-2}, 10 Hz) to ablate a polycrystalline $BaTiO_3$ target (Sakai Chemical Industry). The substrate temperature was 750 °C and the oxygen partial pressure was 1.0 Pa. A deposition time of 65 min yielded a film thickness of ~50 nm. Out-of-plane XRD and X-ray reflectivity (XRR) measurements were performed using a Rigaku SmartLab with monochromated Cu $K\alpha_1$ radiation to evaluate the crystal structure and film thickness, respectively. Nitridation of the $BaTiO_3$ film was conducted with 0.2 g of Ca_3N_2 in a sealed, evacuated Pyrex tube at 550 °C for 2 weeks. After cooling, the

film was washed with 0.1 M NH_4Cl/MeOH to remove excess Ca_3N_2 powder and the CaO byproduct from the surface.

XPS depth profiling was conducted using a PHI Quantera II (Al Kα, 1486.6 eV; analysis area 100 μm diameter; take-off angle 45°) with Ar^+ sputtering at 2.0 kV. Spectra of Ba $3d_{5/2}$, Ti 2p, O 1s, N 1s, and Mg 1s were recorded to quantify Ba, Ti, O, N, and Mg as a function of sputter time. Possible sputter-induced compositional changes were considered, and comparisons were made assuming similar sputter damage among samples.

The electrode substrate was a fluorine-doped tin oxide (FTO) cleaned with acetone. 5 mg of $BaTiO_3$ and $BaTiO_{3-3x/2}N_x$ were added to a mixture of 0.7 mL of EtOH and 0.3 mL of H_2O, and the catalyst ink was prepared by sonication. The FTO electrode was heated to approximately 373 K on a hot plate while drops of catalyst ink were applied to ensure uniformity. The apparent catalyst coverage was 2.0 cm^{-2}. The electrodes were dried overnight at 343 K in air. Photoelectrochemical measurements were carried out with a potentiostat (HZ-Pro, Hokuto Denko) and an electrochemical cell at ~298 K. A three-electrode system was used with a Pyrex glass cell, platinum wire and Ag/AgCl (−0.059 pH, −0.198 V *vs.* RHE, 298 K) electrodes as counter and reference electrodes, respectively (Fig. S10). An aqueous 0.1 M Na_2SO_4 (Wako, > 99.0%) solution of pH 5.9 was used as the electrolyte. Before the electrochemical measurements, the electrolyte was saturated with Ar gas. The light source was a 300 W Xe lamp (PE300BF, Cermax) fitted with an L42 cut-off filter (HOYA). All LSV measurements were conducted at a sweep rate of 20 mV s^{-1}.

Author contributions

Y. S. and H. K. designed the study. Y. S. and K. Y. synthesized samples and performed structural characterization; K. Y., D. K., and I. Y. conducted optical and photocatalytic measurements; Y. S. and Y. T. carried out photoluminescence and electron paramagnetic resonance measurements; K. Mo. measured the morphology; Hik. T., T. T., and Hir. T. measured soft X-ray absorption spectroscopy. S. H., S. S., and K. Ma. contributed to discussions. Y. S. and H. K. wrote the manuscript with the aid of all co-authors.

Conflicts of interest

The authors declare no competing financial interest.

Data availability

Additional data are available from the corresponding author upon reasonable request.

Supplementary information (SI): additional XRD, UV-vis/PL, Ti valence analyses (EPR, XAS), nitrogen-content analyses, reaction time and particle size dependence, depth profiling, photoelectrochemical measurements, and tables. See DOI: https://doi.org/10.1039/d6sc00009f.

Acknowledgements

This work was supported by JST CREST (JPMJCR20R2), JST ASPIRE (JPMJAP2408), JST PRESTO (JPMJPR21Q5), and JSPS KAKENHI (JP22H04914, JP22H05143, JP22H05148, JP23KJ1151). The XAS experiments were performed at the BL-12A of KEK (2025G532). We thank T. Ohigashi for assistance with the XAS measurement and T. Yoshii, S. Shimizu, Z. Tong, K. Murayama, S. Yoshida, T. Yoshimura, R. Terada, and A. Gabov for fruitful discussions and technical support. VESTA was used to visualize crystal structures.[37]

Notes and references

1 H. Kageyama, K. Hayashi, K. Maeda, J. P. Attfield, Z. Hiroi, J. M. Rondinelli and K. R. Poeppelmeier, *Nat. Commun.*, 2017, **9**, 772.
2 A. Fuertes, *Mater. Horiz.*, 2015, **2**, 453.
3 R. Asahi, T. Morikawa, T. Ohwaki and K. A. Y. Taga, *Science*, 2001, **293**, 269.
4 M. Jansen and H. P. Letschert, *Nature*, 2000, **404**, 980.
5 Y. Bao, C. Li, K. Domen and F. Zhang, *Acc. Mater. Res.*, 2022, **3**, 449.
6 K. Maeda, *Prog. Solid State Chem.*, 2018, **51**, 52.
7 Y. Kim, P. M. Woodward, K. Z. Baba-Kishi and C. W. Tai, *Chem. Mater.*, 2004, **16**, 1267.
8 D. Oka, Y. Hirose, H. Kamisaka, T. Fukumura, K. Sasa, S. Ishii, H. Matsuzaki, Y. Sato, Y. Ikuhara and T. Hasegawa, *Sci. Rep.*, 2014, **4**, 4987.
9 S. Chen, J. Chen, G. Feng, H. Zhang and W. Fan, *Int. J. Hydrogen Energy*, 2024, **80**, 82.
10 A. H. White and W. Melville, *J. Am. Chem. Soc.*, 1905, **27**, 373.
11 J. Yu, L. Shi, R. Li, J. Huang, R. Wang, Z. Li, C. Shen, G. Liu, Y. Li and X. Xu, *ACS Catal.*, 2024, **14**, 608.
12 T. Yajima, F. Takeiri, K. Aidzu, H. Akamatsu, K. Fujita, W. Yoshimune, M. Ohkura, S. Lei, V. Gopalan, K. Tanaka, C. M. Brown, M. A. Green, T. Yamamoto, Y. Kobayashi and H. Kageyama, *Nat. Chem.*, 2015, **7**, 1017.
13 A. Gomathi, S. Reshma and C. N. R. Rao, *J. Solid State Chem.*, 2009, **182**, 72.
14 Y. Masubuchi, M. Tadaki and S. Kikkawa, *Chem. Lett.*, 2018, **47**, 31.
15 R. Okada, K. Katagiri, Y. Masubuchi and K. Inumaru, *Eur. J. Inorg. Chem.*, 2019, **2019**, 1257.
16 Q. Yang, Y. Masubuchi and M. Higuchi, *Ceram. Int.*, 2020, **46**, 13941.
17 M. Sakar, R. M. Prakash, K. Shinde and G. R. Balakrishna, *Int. J. Hydrogen Energy*, 2020, **45**, 7691.
18 *CRC Handbook of Chemistry and Physics*, 93rd edn, ed. W. M. Haynes, D. R. Lide and T. J. Bruno, CRC Press, Boca Raton, FL, 2012.
19 T. Bräuniger, T. Müller, A. Pampel and H.-P. Abicht, *Chem. Mater.*, 2005, **17**, 4114.
20 Y. Ye, M. Kapilashrami, C. H. Chuang, Y. S. Liu, P. A. Glans and J. Guo, *MRS Commun.*, 2017, **7**, 53.
21 T. Tsumura, K. Matsuoka and M. Toyoda, *J. Mater. Sci. Technol.*, 2010, **26**, 33.

22 J. Lee, H. Jeong and S. Ma, *Mater. Res. Express*, 2022, **9**, 065001.
23 T.-C. Huang, M.-T. Wang, H.-S. Sheu and W.-F. Hsieh, *J. Phys. Condens. Matter*, 2007, **19**, 476212.
24 M. A. Hayward, E. J. Cussen, J. B. Claridge, M. Bieringer, M. J. Rosseinsky, C. J. Kiely, S. J. Blundell, I. M. Marshall and F. L. Pratt, *Science*, 2002, **295**, 1882.
25 Y. Kobayashi, O. J. Hernandez, T. Sakaguchi, T. Yajima, T. Roisnel, Y. Tsujimoto, M. Morita, Y. Noda, Y. Mogami, A. Kitada, M. Ohkura, S. Hosokawa, Z. Li, K. Hayashi, Y. Kusano, J. Kim, N. Tsuji, A. Fujiwara, Y. Matsushita, K. Yoshimura, K. Takegoshi, M. Inoue, M. Takano and H. Kageyama, *Nat. Mater.*, 2012, **11**, 507.
26 Y. Kobayashi, O. Hernandez, C. Tassel and H. Kageyama, *Sci. Technol. Adv. Mater.*, 2017, **18**, 905.
27 GHS Material Safety Data Sheet, SDS No. : VVI01PAEG", https://www.kojundo.co.jp/dcms_media/other/VVI01PAEG.pdf?_ga=2.174203106.1147913147.1760103682-728587727.1760103682, (accessed December 2025).
28 M. Laing, *J. Chem. Educ.*, 2001, **78**, 1054.
29 C. L. Rom, A. Novick, M. J. McDermott, A. A. Yakovenko, J. R. Gallawa, G. T. Tran, D. C. Asebiah, E. N. Storck, B. C. McBride, R. C. Miller, A. L. Prieto, K. A. Persson, E. Toberer, V. Stevanović, A. Zakutayev and J. R. Neilson, *J. Am. Chem. Soc.*, 2024, **146**, 4001.
30 A. Hartl, J. Minár, P. Constantinou, V. Roddatis, F. Alarab, A. M. Müller, C. Vockenhuber, T. Schmitt, D. Pergolesi, T. Lippert, V. N. Strocov and N. A. Shepelin, *Chem. Mater.*, 2024, **36**, 11393.
31 T. Takata, J. Jiang, Y. Sakata, M. Nakabayashi, N. Shibata, V. Nandal, K. Seki, T. Hisatomi and K. Domen, *Nature*, 2020, **581**, 411.
32 R. Li, T. Takata, B. Zhang, C. Feng, Q. Wu, C. Cui, Z. Zhang, K. Domen and Y. Li, *Angew. Chem., Int. Ed.*, 2023, **135**, e202313537.
33 N. Hirayama, H. Nakata, H. Wakayama, S. Nishioka, T. Kanazawa, R. Kamata, Y. Ebato, K. Kato, H. Kumagai, A. Yamakata, K. Oka and K. Maeda, *J. Am. Chem. Soc.*, 2019, **141**, 17158.
34 S. Akiyama, M. Nakabayashi, N. Shibata, T. Minegishi, Y. Asakura, M. Abdulla-Al-Mamun, T. Hisatomi, H. Nishiyama, M. Katayama, T. Yamada and K. Domen, *Small*, 2016, **12**, 5468.
35 T. Higashi, H. Nishiyama, V. Nandal, Y. Pihosh, Y. Kawase, R. Shoji, M. Nakabayashi, Y. Sasaki, N. Shibata and H. Matsuzaki, *Energy Environ. Sci.*, 2022, **15**, 4761.
36 V. Petříček, M. Dušek and L. Palatinus, *Z. Kristallogr. Cryst. Mater.*, 2014, **229**, 345.
37 K. Momma and F. Izumi, *J. Appl. Crystallogr.*, 2011, **44**, 1272.